A Thermodynamic Framework for Quantifying Firn Thermal Evolution: Cold Content Depletion, Energy Barrier Reduction and Thermal Commitment of Austfonna Ice Cap, Svalbard (2009-2022)

Geetha Priya M*, Adithya Sunil
Centre for Incubation, Innovation, Research and Consultancy, Jyothy Institute of Technology, Bengaluru-560082.
*geetha.sri82@gmail.com

A Thermodynamic Framework for Quantifying Firn Thermal Evolution: Cold Content Depletion, Energy Barrier Reduction and Thermal Commitment of Austfonna Ice Cap, Svalbard (2009-2022)

Geetha Priya M*, Adithya Sunil
Centre for Incubation, Innovation, Research and Consultancy (CIIRC), Jyothy Institute of Technology, Bengaluru-560 082.
*geetha.sri82@gmail.com

Abstract

Svalbard is warming several times faster than the global mean, yet most glaciological studies characterise firn thermal change through temperature trends alone rather than the underlying thermodynamic state. This study develops a linked diagnostic framework, cold content (CC_{col}), energy barrier ($EB_{relative}$), advective Péclet number (Pe_{adv}), and thermal relaxation time (τ) and applies it to a 14-year borehole temperature record (2009-2022) from the summit of Austfonna Ice Cap, Svalbard, providing the first continuous multiyear thermodynamic characterisation of this ice cap derived directly from borehole temperature observations rather than a forcing driven model. After correction for multiple comparisons, warming remained significant at 8-10 m using all available years and at 3-10 m using complete years. Near surface trends remained large but statistically uncertain. Between the 2010-2013 reference period and the 2020-2022 late post transition period, mean cold content declined from 9.964 to 4.653 MJ m^{-2} (53.3%, -562 kJ m^{-2} yr^{-1}, R^2=0.57, p=0.007), and the energy barrier fell to 46.7% of its pre transition reference value. Under the reference whole column ice equivalent scaling, Pe_{adv} was 8.0, while an alternative scaling based on the assumed mean firn density gave Pe_{adv} = 11.3. CC_{col}, $EB_{relative}$ are calculated consistently and can be compared between periods. In contrast, Pe_{adv} and τ provide site scale context and remain unchanged between periods unless the prescribed values of H, b, or α are updated. Comparisons between sites therefore require consistent parameter definitions and characteristic length scales. Requiring a borehole temperature record, a representative density profile, an accumulation rate estimate, an ice thickness estimate, and a reference thermal diffusivity, the framework is substantially less data intensive than coupled energy balance models and is broadly transferable to other polythermal ice masses beyond the site studied here.

Keywords: Polythermal glacier thermodynamics, cold content, energy barrier, Péclet number, thermal relaxation time, firn temperature, meltwater refreezing, Svalbard.

1. Introduction

Svalbard is warming faster than almost anywhere else on Earth. At Svalbard Airport, annual mean air temperature increased by approximately +1.7 °C decade^{-1} during 1991-2018, more than twice the Arctic average and approximately seven times the global mean warming rate over the same period (Nordli et al., 2020). This rapid atmospheric warming has fundamentally altered the thermal and hydrological structure of Arctic firn through enhanced surface melt, increased meltwater percolation, and intensified latent heat release during refreezing (Cuffey and Paterson, 2010; Benn and Evans, 2010). The resulting reduction in firn pore space, increase in density, and modification of internal temperature profiles directly influence glacier mass balance, runoff generation, and dynamic response. Most investigations of these processes, however, describe glacier thermal evolution primarily through temperature trends, mean annual firn temperatures, or the timing of cold to temperate transitions inferred from borehole observations (Cuffey and Paterson, 2010).

Temperature, however, is an observable rather than a complete descriptor of the thermodynamic state of a glacier. Two firn columns experiencing similar warming trends may nevertheless differ substantially in the amount of energy required to reach a fully temperate state, a distinction that depends on both temperature and density through the internal energy stored within the firn column. Cold content has therefore become an increasingly valuable metric for quantifying firn thermal state and melt buffering at decadal timescales (Vandecrux et al., 2020). Nevertheless, cold content has generally been analysed as an isolated quantity rather than as part of an integrated thermodynamic description linking energy storage, heat transfer mechanisms, and long term thermal adjustment.

Austfonna Ice Cap, the largest ice cap in the Svalbard archipelago, provides one of the longest continuous borehole temperature records presently available from the Arctic accumulation zone, spanning 2009-2022 at a summit site (773 metres above sea level (m a.s.l.)). The most comprehensive analysis of this record, by Innanen et al., (2025b), combined borehole observations with sixteen firn cores and CryoGrid simulations to demonstrate that Austfonna underwent a transition from cold to temperate firn in 2013, driven primarily by enhanced meltwater percolation and latent heat release during refreezing. Their study established both the timing and physical mechanism of this transition and also presented a model derived annual cold content series for the upper 10 m of firn. Because that model derived series covers the upper 0-10 m, whereas the present observational diagnostic covers 4-

10 m, their cold content trends are not directly comparable. That series exhibits pronounced interannual variability but no statistically significant long term trend. The outstanding question is therefore not whether the transition occurred, but whether a borehole derived cold content record exhibits statistically significant depletion and whether that depletion can be interpreted quantitatively in terms of changing thermal resistance, dominant heat transfer mechanisms, and long term thermal adjustment. Schuler et al., (2014) presented eight years of meteorological observations from Austfonna but did not investigate the accompanying subsurface thermal evolution recorded by the borehole. Neither study quantified a cold content based Energy Barrier, a Péclet number describing whole column advection diffusion scaling, or a characteristic thermal relaxation timescale for the Austfonna firn column.

To address this gap, we use four linked thermodynamic quantities: CC_{col}, $EB_{relative}$, Pe_{adv} and τ. CC_{col} and $EB_{relative}$ are time varying diagnostics derived from the annual temperature profiles. In contrast, Pe_{adv} and τ are scale parameters calculated from the prescribed values of H, b, and α, and therefore remain constant in the present analysis. Climatic warming and meltwater refreezing can reduce CC_{col}, $EB_{relative}$, whereas Pe_{adv} provides whole column advection diffusion context and τ provides an idealized full column conductive response timescale (Cuffey and Paterson, 2010; Robin, 1955). The four quantities are therefore interpreted according to their distinct roles rather than as four independently evolving state variables.

Accordingly, this study has four descriptive objectives: (1) quantify annual CC_{col} and $EB_{relative}$ and compare the 2010-2013 reference period with explicitly defined post transition subsets; (2) compare these diagnostics with depth resolved temperature trends and zero curtain duration; (3) calculate Pe_{adv} as a fixed whole column scaling parameter under the prescribed site assumptions; and (4) calculate τ as an idealized full depth conductive timescale and evaluate empirical cold content depletion pathways. Because $EB_{relative}$ is normalized CC_{col} and Pe_{adv} and τ remain fixed under the prescribed parameters, these quantities are not treated as independent hypothesis tests or as evidence of a temporal change in heat transfer regime.

2. Study Site and Data

Austfonna is the largest ice cap in the Svalbard archipelago and one of the largest ice masses in the Eurasian Arctic, located on Nordaustlandet in northeastern Svalbard (Figure 1). The ice cap covers approximately 8,105 km² (Schuler et al., 2014) and extends from sea level to the summit dome at 783 m a.s.l., where airborne radio echo sounding indicates a maximum ice thickness of approximately 560 m (Dowdeswell et al., 1986; Schuler et al., 2014). Austfonna is a low relief, dome shaped ice cap drained by a series of marine and land terminating outlet glaciers and ice streams radiating from the summit dome, and it spans both a maritime influenced southern margin and a more continental interior accumulation zone. The summit region, where the Camp borehole site is located, lies within the ice cap's accumulation zone and is characterised by a polythermal thermal regime cold firn overlying temperate ice that has been the subject of longstanding glaciological interest given its sensitivity to Svalbard's rapidly warming climate (Dowdeswell et al., 1986; Nordli et al., 2020). Mean annual accumulation at the summit is estimated at 0.45 m w.e. yr^{-1} (Taurisano et al., 2007), placing the site within a moderate accumulation regime relative to other high Arctic ice caps.

Firn temperatures at the summit site (Camp; 773 m a.s.l., 79.85289°N, 23.79802°E) have been monitored continuously since May 2009 by the University of Oslo and the Norwegian Polar Institute using three successive thermistor string deployments (Figure 1). The borehole is located at 773 m a.s.l., near the summit dome (783 m a.s.l.), with a maximum dome ice thickness of approximately 560 m. Full deployment dates, sensor counts, logger models, and accuracy specifications are summarised in Supplementary Table S1. Briefly, the record spans three sequential deployments between 2009 and 2022, with sensor accuracy of ±0.1-0.2°C depending on deployment, and an approximately eight month data gap between 28 August 2018 and 26 April 2019 owing to logger memory capacity being exceeded. Together, these three deployments provide a near continuous 14-year borehole temperature record (2009-2022), forming the observational basis for all analyses presented in this study. The present study uses these archived borehole observations (Norwegian Polar Institute Data Centre, DOI: 10.21334/NPOLAR.2025.10DB6623) while applying a new thermodynamic diagnostic that was not part of the original analysis by (Innanen et al., 2025b). Because thermistors moved relative to the evolving firn surface through time, the depth of each sensor relative to the surface was reconstructed using surface height changes simulated by the CryoGrid community land model (Schmidt et al., 2023; Westermann et al., 2023), following the procedure adopted in the

original characterisation of the dataset. CryoGrid derived surface height was used solely to determine the evolving depth of each thermistor within the firn column and was not otherwise incorporated into the thermodynamic analyses presented here. Following depth correction, temperature observations were interpolated onto a fixed vertical grid.

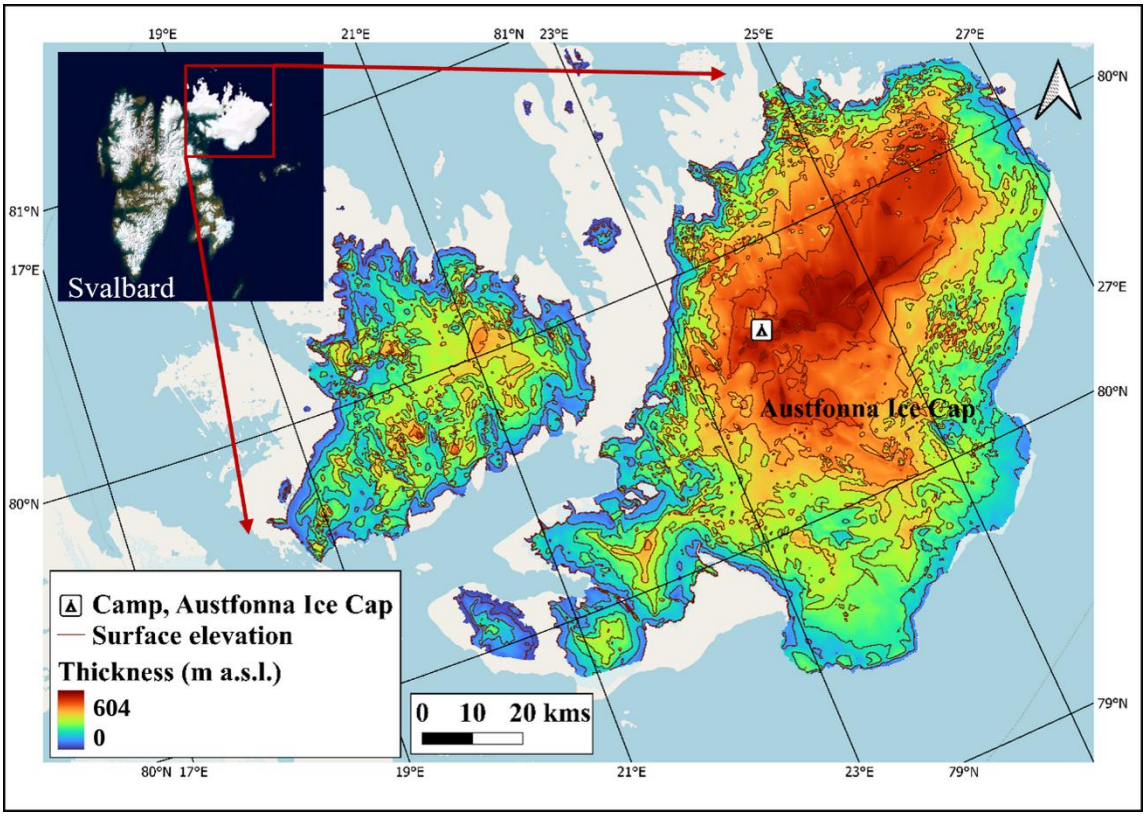


Figure 1. Study area and borehole location, including a Svalbard regional inset, Austfonna outline with ice thickness 70 m interval contours (ArcticDEM 2023), Camp, Austfonna Ice Cap, Svalbard (79.85289°N, 23.79802°E).

Firn density, required for the cold content calculations and depth dependent thermal property estimates, was not measured continuously at the Camp site. A reference density profile was therefore constructed from the nearest and most temporally representative density depth measurements available from the co located Summit_2012 firn core (Innanen et al., 2025a), consistent with the initialisation adopted in previous CryoGrid applications for Austfonna. Owing to the absence of repeated density measurements, this profile was assumed to remain temporally invariant throughout the study period. Consequently, the analysis quantifies temperature driven changes under a fixed density structure and does not simulate temporal densification caused by compaction or refreezing.

3.Methods

The adopted process flow is shown in Figure 2. Briefly, quality controlled thermistor observations are interpolated onto a fixed vertical grid, from which depth dependent thermal properties, cold content, conductive heat flux, and seasonal thermal wave characteristics are derived. These outputs feed a set of four linked thermodynamic state variables, cold content, energy barrier, advective Péclet number, and thermal relaxation time. Cold content additionally underpins future thermal commitment projections.

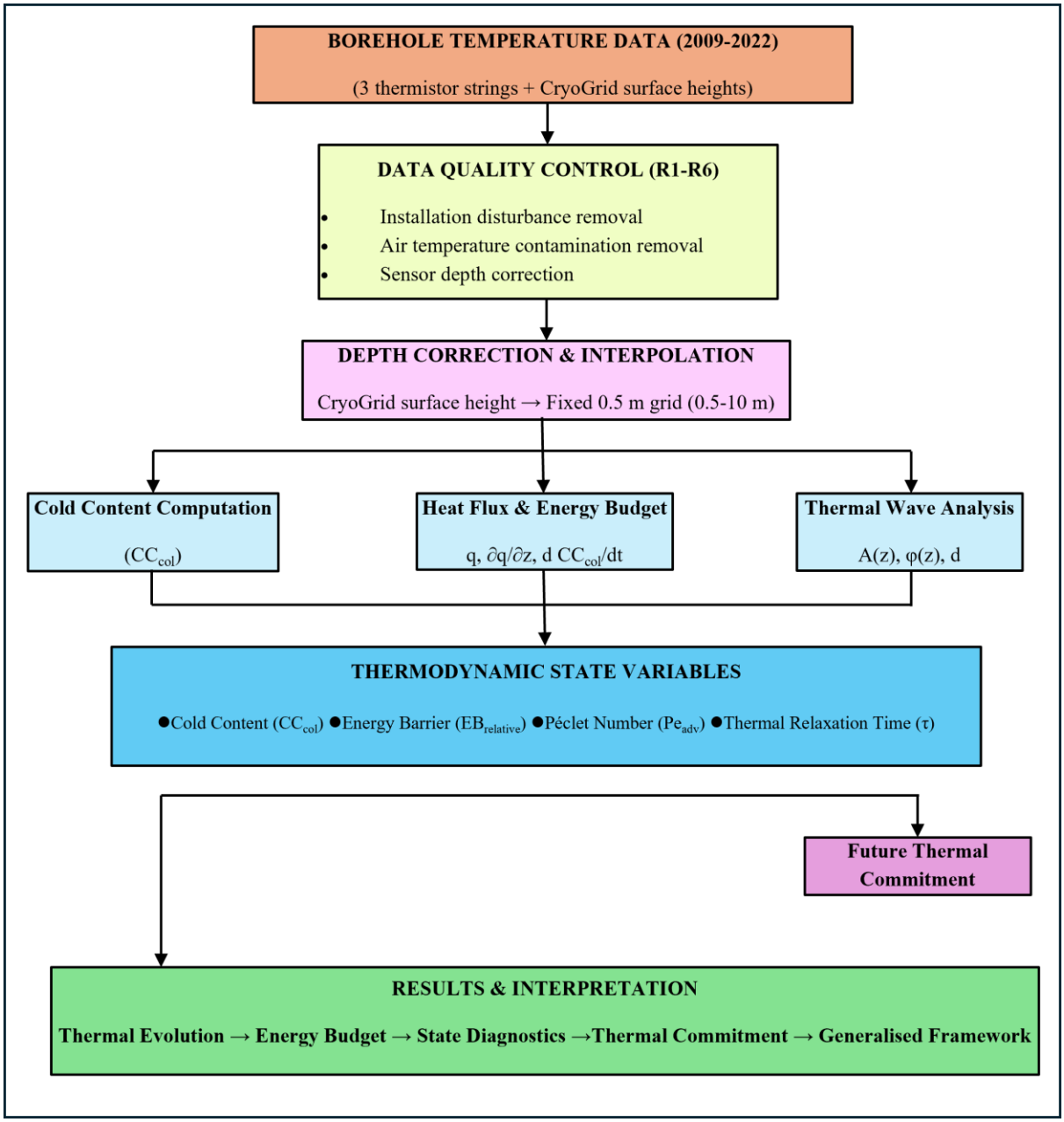


Figure 2. Workflow of the thermodynamic framework for borehole temperature processing, heat transfer analysis, and thermal state diagnostics.

3.1 Data quality control

Before interpolation and thermodynamic analysis, the borehole temperature observations were processed following the quality control workflow provided with the source dataset. Five correction stages were applied: (1) reconstruction of thermistor depth relative to the CryoGrid simulated surface; (2) removal of observations from thermistors positioned above the modelled firn surface; (3) removal of observations identified as air temperature contamination; (4) exclusion of approximately two months of data following each thermistor string installation; and (5) sensor specific correction of zero offset biases identified from stable melt season temperature plateaus. Where zero offset correction produced temperatures above the melting point, those values were constrained to 0 °C. The resulting quality controlled temperature record was then imported into the input workbook for subsequent interpolation and thermodynamic analysis. Full correction details are provided in Supplementary Table S2.

3.2 Temperature grid interpolation

Depth dependent firn thermal conductivity, $k_{firn}(\rho)$, was derived from the reference density profile using the Calonne et al., (2011) parameterisation and was used in the conductive heat flux calculation. Firn thermal diffusivity was calculated as $\alpha_{firn}(z) = k_{firn}(z)/[\rho(z)c]$, and its mean over the 4-10 m analysis window was used only for the theoretical thermal wave penetration depth benchmark. Following quality control, corrected thermistor observations were interpolated daily onto a fixed vertical grid extending from 0.5 to 10 m below the evolving firn surface at 0.5 m intervals (20 nodes). Linear interpolation was performed between the two nearest valid thermistors at each time step. Where the shallowest valid sensor was located below 0.5 m, temperature was extended upward as a constant over intervals not exceeding 1 m. No extrapolation was performed below the deepest valid thermistor; values outside the observed depth range were treated as missing. This interpolation provides a temporally consistent vertical temperature field that is independent of the changing physical positions of individual thermistors and forms the basis for all subsequent thermodynamic calculations.

3.3 Cold content computation

Cold content per unit surface area was computed as

$$CC_{col} = \int_{z_1}^{z_2} \rho(z) c [T_f - T(z)]\, dz \qquad (1)$$

where $\rho(z)$ is the depth dependent firn density, c is the specific heat capacity of ice, T_f is the melting temperature (0 °C), and T(z) is the observed firn temperature.

Integration was performed over the primary 4-10 m analysis window using trapezoidal integration across the thirteen 0.5 m grid nodes spanning this interval. Annual cold content was computed using monthly mean temperatures. Months containing at least 15 valid daily profiles contributed to the annual calculation, and annual values were retained only when at least 10 monthly means were available. Physically, cold content represents the thermal energy that must be supplied to warm the firn column to the melting point before additional energy can produce melt, and therefore provides a measure of the remaining thermal memory of the firn column.

3.4 Conductive heat flux diagnostics

Conductive heat flux was calculated as $q(z) = -k(z)\partial T/\partial z$ using the depth varying thermal conductivity and the interpolated temperature gradient. Its vertical gradient, $\partial q/\partial z$, was retained only as a descriptive measure of conductive flux convergence and divergence. Because the analysis did not solve a complete energy balance or invert for an internal source term, $\partial q/\partial z$ was not converted to a local energy storage rate and was not interpreted as latent heat release. The annual change in column cold content was evaluated separately from the annual cold content series.

3.5 Thermal wave analysis

At each grid depth, the period composite seasonal cycle was fitted by ordinary least squares as $T(z,t) = \bar{T}(z) + \beta c(z)\cos(\omega t) + \beta s(z)\sin(\omega t)$, where $\omega = 2\pi/365.25$ days and t is the fractional day of year. Fits were performed separately for 2009-2013 and 2014-2022 using all valid daily observations with equal weighting; partial years contributed only their available daily observations. Seasonal amplitude was calculated as $A(z) = \sqrt{[\beta c^2 + \beta s^2]}$, and phase was unwrapped with depth and expressed relative to the 0.5 m grid node. Because corrected temperatures above 0 °C were constrained to the melting point during quality control, the fitted amplitude and phase values are interpreted as descriptive first harmonic summaries; melting point plateaus, particularly at shallow depths, may reduce fitted amplitudes and influence phase estimates.

The theoretical thermal penetration depth (Carslaw and Jaeger, 1959) was calculated as

$$d = \sqrt{\frac{2\alpha}{\omega}} \tag{2}$$

where α is thermal diffusivity and

$$\omega = \frac{2\pi}{365.25 \text{ days}} \quad (3)$$

The amplitude derived damping depth, dA, was obtained from $A(z) = A(0.5) \times \exp[-(z-0.5)/d_A]$, while the phase derived characteristic depth, dφ, was obtained from $\Delta\varphi(z) = (z-0.5)/d\varphi$. Both quantities were derived from the period composite fits rather than annual estimates.

3.6 Period definitions and statistical analysis

Period terminology was defined according to the purpose and data completeness requirements of each analysis. The year 2013 was treated as the independently identified transition year. The term 'post transition period' refers generally to observations from 2014 onwards. When a calculation used a subset of these years, the exact years are stated explicitly. The 2020-2022 mean used for the cold content comparison is referred to as the 'late post transition mean' and not as the mean of the entire post transition period. Complete year zero curtain comparisons use 2010-2013 as the reference period and 2016-2017 plus 2020-2022 as the complete post transition subset. Temporal trends were evaluated using ordinary least squares regression. Cold content trend robustness was assessed using the Theil-Sen median slope estimator, the Mann-Kendall trend test, leave one year out regression and the Durbin-Watson statistic for first order residual autocorrelation. For the 20 depth wise temperature regressions, p values were adjusted separately for the all available year and complete calendar year analyses using the Benjamini-Hochberg false discovery rate (FDR) procedure, with $q < 0.05$ considered statistically significant.

3.7 Thermodynamic state variables

Four complementary thermodynamic descriptors were derived, using the physical constants and variable definitions summarised in Supplementary Tables S3 and S4 respectively.

Cold Content (CC_{col})

Cold content was calculated as described in Section 3.3.

Energy Barrier ($EB_{relative}$)

The Energy Barrier is introduced here as a relative diagnostic index, defined as

$$EB_{relative} = \frac{CC_{period}}{CC_{reference}} \times 100 \quad (4)$$

where the reference period corresponds to the pre transition state.

Normalisation permits comparison between periods independent of the absolute magnitude of cold content and expresses the remaining thermal resistance of the firn column relative to its initial condition.

Advective Péclet Number

The advective Péclet number was computed as,

$$Pe_{adv} = \frac{wH}{\alpha} \quad (5)$$

following the classical vertical advection formulation (Cuffey and Paterson, 2010; Robin, 1955). For the reported Pe_{adv} calculations, $\alpha = \alpha_{ice}$ denotes the pure ice reference thermal diffusivity listed in Supplementary Table S3; it is not a depth averaged firn diffusivity. Here, the surface accumulation rate was converted to ice equivalent velocity as

$$w_{ice} = \frac{b\rho_w}{\rho_{ice}} \quad (6)$$

where b is the surface accumulation rate, ρ_w is water density, and ρ_{ice} is pure ice density. In Equation (5), H = 560 m represents the estimated full ice thickness at the summit, and α is the pure ice reference thermal diffusivity. Consequently, Pe_{adv} is used as a whole column scaling diagnostic and not as a local Péclet number for the 4-10 m observational window. Conversion of the accumulation rate to ice equivalent velocity gives w_{ice} = 0.491 m yr^{-1} and a reference whole column Pe_{adv} of 8.0. As a density conversion sensitivity, the accumulation rate was also converted using the assumed mean firn density of 650 kg m^{-3}, giving a near surface firn burial velocity of 0.692 m yr^{-1} and Pe_{adv} = 11.3. The latter is retained only as a sensitivity estimate and is not treated as an ice equivalent velocity. Neither value varies annually or is used to infer a temporal change in heat transfer regime.

Thermal Relaxation Time

The characteristic conductive response time of the ice column was estimated as,

$$\tau = \frac{H^2}{\pi^2 \alpha} \quad (7)$$

Equation (7) represents the fundamental conductive diffusion timescale for a one-dimensional slab of thickness H, assuming prescribed temperature perturbations at the upper and lower boundaries and the pure ice reference diffusivity α used for Pe_{adv} (Carslaw and Jaeger, 1959). Alternative boundary conditions would change the numerical coefficient. Using H=560 m gives τ =926 years. For comparison, applying the same scaling to characteristic lengths of 10 m and 6 m gives approximately 0.30 and 0.11 years, respectively. These shorter values are scale comparisons only and not measured local equilibration times.

4. Results

4.1. Thermal Characterisation

4.1.1 Depth resolved warming trends

Ordinary least squares regression was applied to the available annual mean temperature estimates at each of the 20 fixed grid nodes spanning 0.5-10 m depth (Figure 3; Supplementary Table S5). Because 2009, 2014, 2015, 2018 and 2019 did not contain 12 valid calendar months, a sensitivity analysis was also performed using only the complete calendar year records: 2010-2013, 2016-2017 and 2020-2022. At 0.5 and 1.0 m, the sample size was further reduced where an annual mean was unavailable. Benjamini-Hochberg false discovery rate correction was applied separately across the 20 depth wise tests in each analysis, with $q < 0.05$ considered statistically significant. In the all available year analysis, unadjusted p values indicated significant warming at 5-10 m. After false discovery rate correction, significant warming was retained at 8-10 m. The strongest trend occurred at 10 m, with a warming rate of +0.89 °C decade^{-1} ($R^2 = 0.60$, $p = 0.001$, $q = 0.025$). The complete calendar year sensitivity analysis retained significant warming from 3 to 10 m after correction, ranging from +1.17 °C decade^{-1} at 3 m to +0.67 °C decade^{-1} at 10 m. The difference between the analyses shows that the depth at which significant warming begins is sensitive to incomplete seasonal coverage.

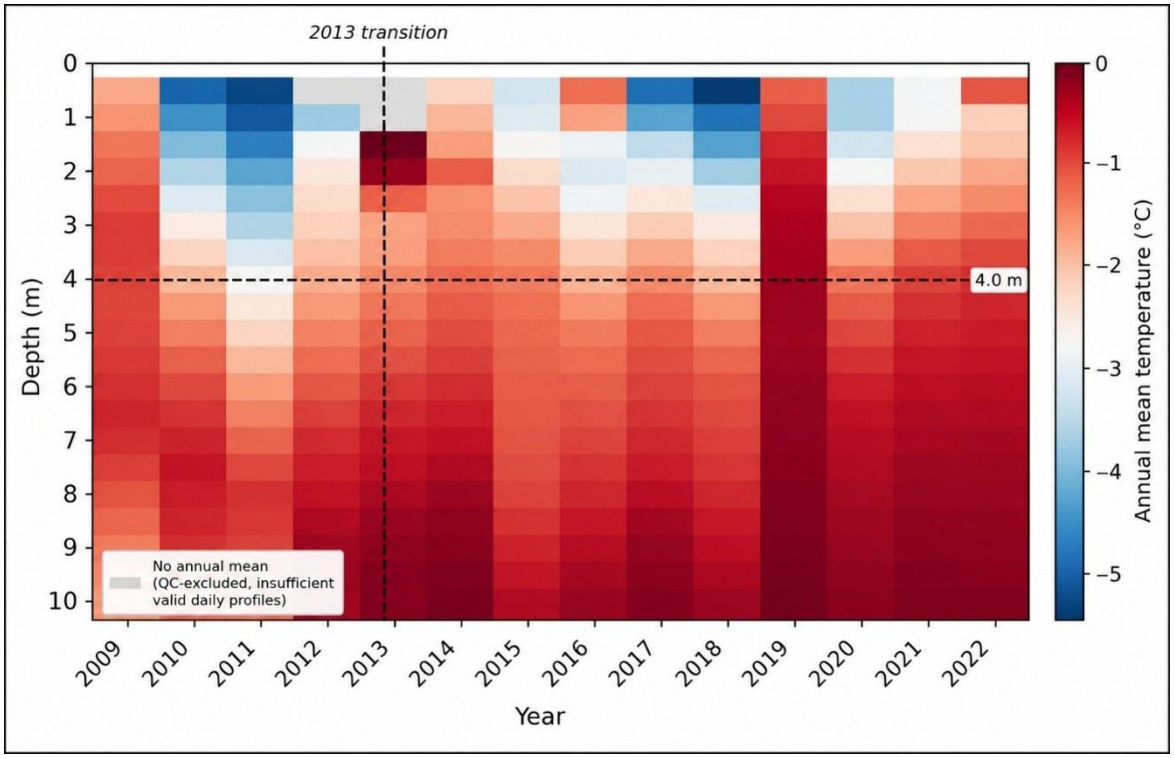


Figure 3. Time depth evolution of annual mean firn temperature (2009-2022), showing the 2013 transition.

4.1.2 Evolution of the vertical temperature structure

Annual mean temperature profiles reveal a generally consistent vertical thermal structure throughout the 2009-2022 observation period (Figure 4). In 12 of the 14-years with sufficient data, the lowest annual mean temperature occurred within the two shallowest analysed depth levels, at either 0.5 or 1.0 m. The minimum occurred specifically at 0.5 m in 10 years and at 1.0 m in two years. In each year, the annual minimum temperature and its corresponding depth were recorded (Supplementary Table S6).

Most annual profiles exhibit a similar shape, characterised by progressively warmer temperatures with increasing depth. This pattern indicates substantial attenuation of seasonal atmospheric forcing within the upper firn column and produces a stable vertical thermal structure during most years of the record. Two years departed from this characteristic profile. In 2013, the annual minimum temperature occurred at 3.0 m depth (-1.805 °C) rather than at the shallowest analysed level. Temperatures above this depth remained close to the melting point, with an annual mean temperature of -0.027 °C at 1.5 m, producing the weakest vertical temperature gradient observed during the study period. A smaller departure occurred in 2016, when the annual minimum temperature was located at 2.0 m depth (-3.164 °C). Following the deeper minima observed at 3.0 m in 2013 and 2.0 m in 2016, the annual minimum occurred at either 0.5 or 1.0 m in every year from 2017 to 2022, indicating a return to the characteristic

vertical temperature structure. The vertical temperature difference between 0.5 m and 10 m, presented as ΔT in Supplementary Table S6, provides a simple measure of annual thermal stratification within the analysed firn column. Years characterised by shallower temperature gradients exhibited smaller vertical temperature differences, whereas years with stronger thermal stratification displayed larger differences between the shallowest and deepest analysed levels.

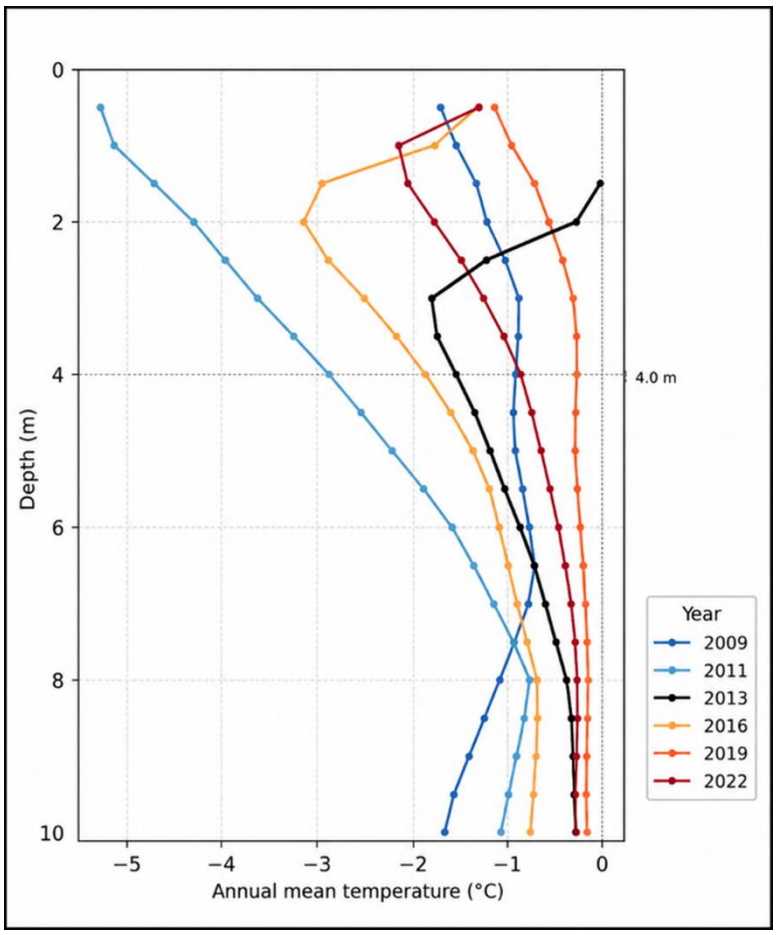


Figure 4. Annual mean temperature depth profiles for selected years (2009, 2011, 2013, 2016, 2019 and 2022).

4.1.3 Zero curtain duration and 0 °C isotherm evolution

The temporal evolution of zero curtain duration and the deepest annual detection of the 0 °C isotherm is shown in Figure 5 and Supplementary Table S7. Temperatures at 4.0 m did not exceed 0 °C, consistent with the physical melting point constraint applied during quality control. Consequently, the thermal state at this depth was evaluated using zero curtain duration rather than the occurrence of positive temperatures. Zero curtain duration at 4.0 m was defined

as the number of valid days per year for which $|T| \leq 0.05$ °C. Using complete calendar year records only, mean zero curtain duration increased from 76.0 days yr^{-1} during the 2010-2013 reference period to 117.6 days yr^{-1} during the complete post transition years 2016-2017 and 2020-2022, corresponding to an increase of approximately 54.7%. The incomplete records from 2009, 2014, 2015, 2018 and 2019 were retained in the annual figure for descriptive purposes but excluded from the period mean comparison. The longest zero curtain duration occurred in 2016, when temperatures at 4.0 m remained within the defined threshold for 146 days. The maximum annual depth of the 0 °C isotherm, z_{vc}, was defined separately as the deepest 0.5 m grid node at which $T \geq 0$ °C occurred on at least one valid day during the year. Consequently, a depth could contribute to zero curtain duration without satisfying the 0 °C isotherm criterion. Between 2009 and 2012, the deepest detected 0 °C grid node increased progressively from 7.0 to 9.5 m. In 2013, the deepest node satisfying this criterion was 2.5 m, although the temperature at 4.0 m remained within $|T| \leq 0.05$ °C for 100 days. These results are not contradictory because zero curtain duration and 0 °C isotherm depth use different temperature criteria. From 2014 onwards, the deepest detected 0 °C node reached the 10 m lower boundary of the interpolation grid in every year. Because 10 m represents the analysis limit rather than the physical lower boundary of the firn column, these values are right censored: the actual maximum depth of the 0 °C isotherm could exceed 10 m.

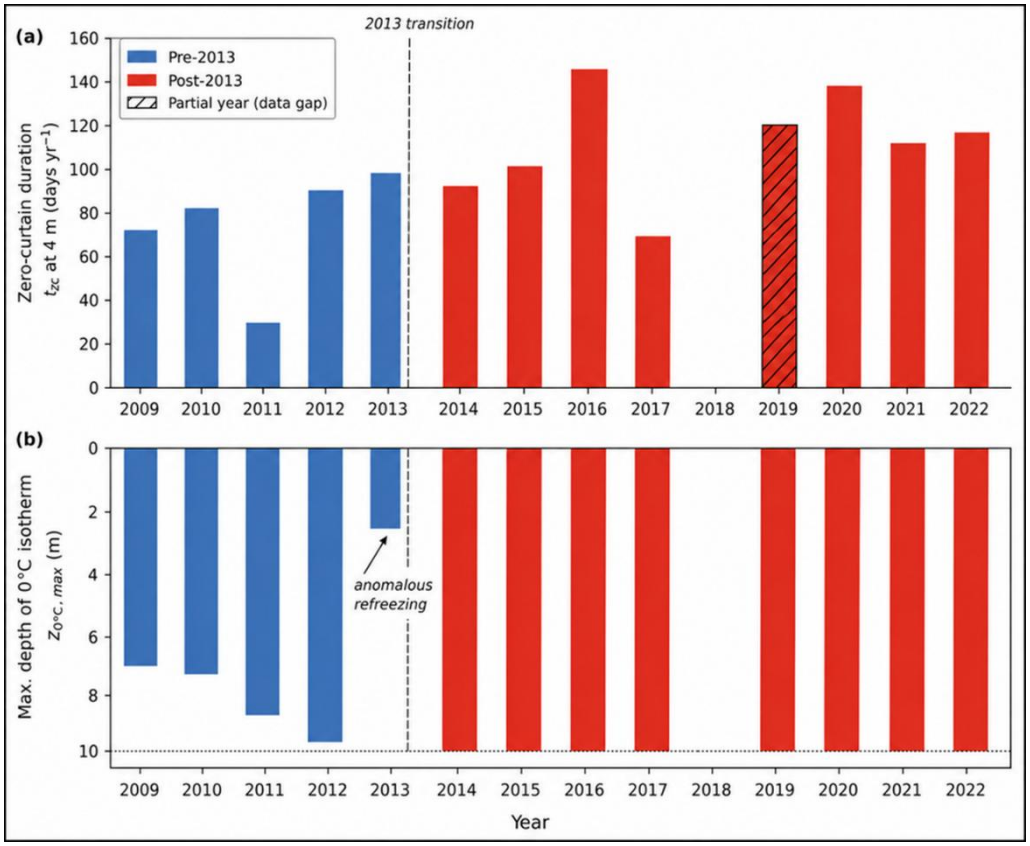
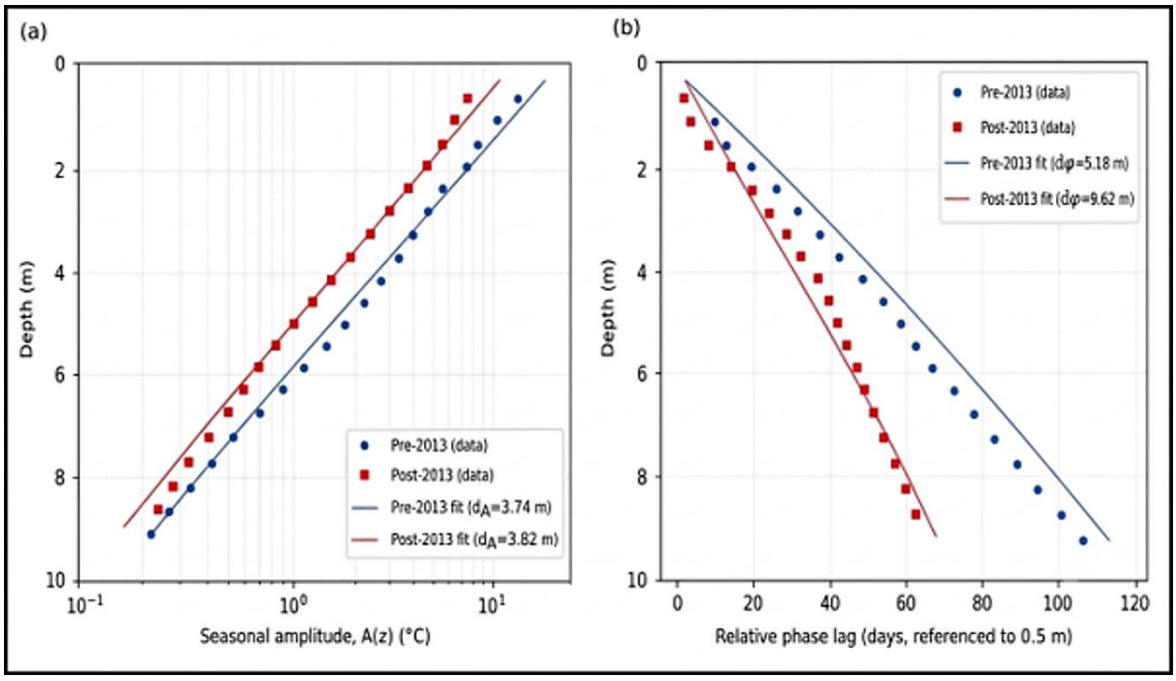


Figure 5. Annual evolution of (a) zero curtain duration at 4.0 m and (b) the deepest detected annual 0 °C grid node during 2009-2022. Incomplete years are identified separately and were excluded from the complete year period mean comparison. Values reaching 10 m are right censored by the lower boundary of the interpolation grid.

4.1.4 Seasonal thermal wave characteristics

Seasonal thermal wave characteristics were quantified from harmonic fits to the daily temperature series at each depth. The resulting amplitude attenuation and phase lag profiles for the pre 2013 (2009-2013) and post 2013 (2014-2022) periods are shown in Figure 6, while the corresponding characteristic parameters are summarised in Table 1. The seasonal temperature amplitude at the shallowest analysed depth (0.5 m) decreased from 5.21 °C during the 2009-2013 period to 3.81 °C during 2014-2022. At 10 m, seasonal amplitudes were substantially smaller, averaging 0.42 °C before 2013 and 0.30 °C afterwards, indicating strong attenuation of the annual temperature signal with depth. Exponential fits to the amplitude profiles produced similar damping depths for the two periods, with 3.74 m before 2013 and 3.82 m after 2013. Using the mean 4-10 m firn thermal diffusivity of 9.34×10^{-7} m^2 s^{-1}, the theoretical conductive

391 penetration depth was approximately 3.1 m. This is smaller than the fitted amplitude damping
392 depths of 3.74 and 3.82 m, indicating that the observed seasonal amplitude attenuated more
393 slowly with depth than predicted by the idealised constant property conductive benchmark. In
394 contrast, characteristic depths derived independently from the harmonic phase lag increased
395 from 5.18 m to 9.63 m between the two periods. Consequently, the ratio of the phase derived
396 characteristic depth to the amplitude derived damping depth increased from 1.39 before 2013
397 to 2.52 afterwards. The amplitude derived damping depth remained similar between periods,
398 whereas the phase derived characteristic depth increased substantially. The divergence between
399 these independently estimated length scales indicates that the observed seasonal signal does
400 not conform completely to the idealised constant property conductive wave benchmark.



401 **Figure 6**. Seasonal thermal wave characteristics before and after 2013: (a) exponential decay
402 of seasonal temperature amplitude with depth and (b) phase lag as a function of depth.

403 **Table 1.** Thermal wave parameters, pre and post 2013

Parameter	**2009-2013**	**2014-2022**
Seasonal amplitude at 0.5 m, A (0.5)	5.21°C	3.81°C
Seasonal amplitude at 10 m, A (10)	0.42°C	0.30°C
Damping depth from amplitude decay, d_A	3.74 m	3.82 m
Characteristic depth from phase lag, d_φ	5.18 m	9.63 m
Ratio d_φ / d_A	1.39	2.52
Theoretical conductive penetration depth, d	3.06m	3.06m

Note: *Seasonal amplitudes and phase lags were obtained from harmonic fits to the daily temperature series. The damping depth (d_A) was estimated from the exponential decay of seasonal amplitude with depth, whereas the characteristic depth (d_φ) was derived independently from the fitted phase lag. Values are reported separately for the 2009-2013 and 2014-2022 periods.*

4.2. Internal Energy diagnostics

4.2.1 Conductive heat flux profiles

Mean conductive heat flux profiles for the pre 2013 (2009-2013) and post 2013 (2014-2022) periods are presented in Figure 7a. The mean conductive heat flux exhibited different depth dependent structures during the two analysis periods. Throughout most of the 4-10 m analysis window, the post 2013 profile remained negative (upward directed), whereas the pre 2013 profile displayed larger magnitudes at depth and crossed zero below approximately 8 m. The greatest difference between the two profiles occurred between approximately 8 and 10 m, where conductive heat flux magnitudes diverged most strongly between the two periods.

4.2.2 Conductive heat flux divergence

The corresponding conductive heat flux divergence profiles are shown in Figure 7b. The vertical conductive heat flux gradient, $\partial q/\partial z$, varied systematically with depth during both analysis periods. Under the adopted sign convention $q = -k\partial T/\partial z$, positive values indicate conductive flux divergence, corresponding to net conductive energy loss, whereas negative values indicate conductive flux convergence, corresponding to net conductive energy gain. These values describe conductive flux convergence and divergence only and are not interpreted as measured local energy storage or latent heat rates. Both period mean profiles exhibited multiple zero crossings rather than maintaining a uniform sign throughout the analysed depth range. Compared with the pre 2013 period, the post 2013 profile showed reduced divergence magnitudes across much of the 5-8 m interval, while retaining a similar overall depth dependent structure.

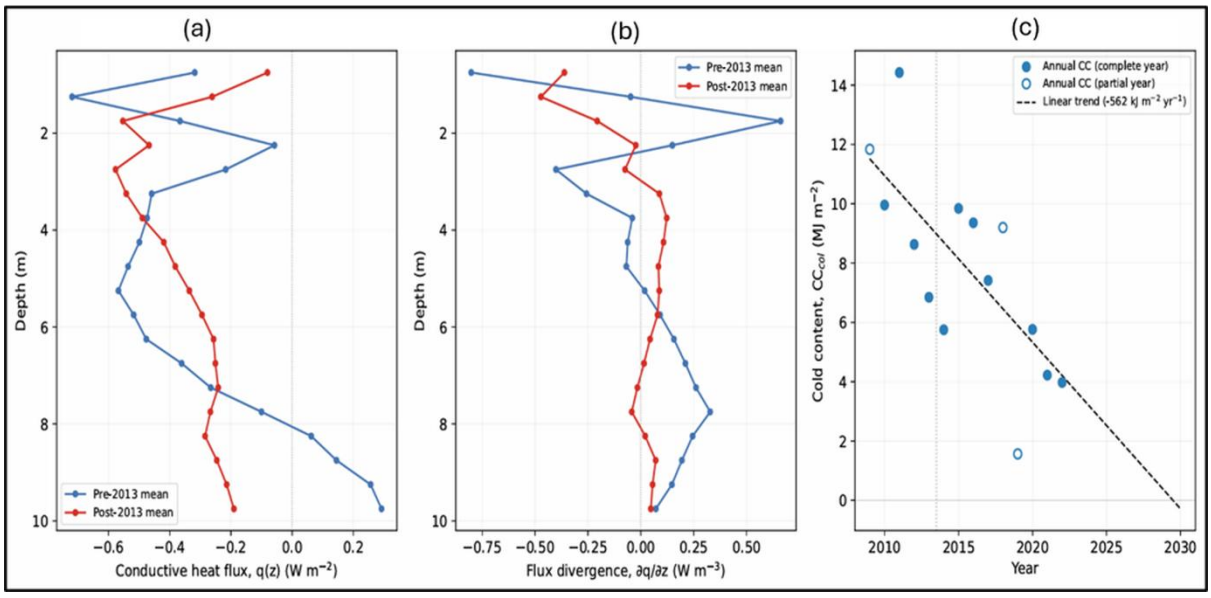
4.2.3 Cold content evolution

Annual cold content values derived from the interpolated temperature profiles are presented in Figure 7c and summarized in Supplementary Table S8. The year 2013 was included in the 2010-2013 reference period mean despite being the transition year identified

by Innanen et al. (2025b). This grouping was used to represent the initial reference state before the lower cold content conditions observed toward the end of the record; it should not be interpreted as a strictly pre transition interval. Cold content varied substantially throughout the observation period, reaching a maximum of 14.424 MJ m^{-2} in 2011 and a value of 3.975 MJ m^{-2} in 2022. Among the annual estimates satisfying the predefined inclusion criterion of at least 10 valid monthly means, mean cold content during the 2010-2013 reference period was 9.964 MJ m^{-2}. Mean cold content during the 2020-2022 late post transition period was 4.653 MJ m^{-2}, representing a reduction of 53.3% relative to the reference period mean. For comparison, the mean across all retained post transition annual estimates, 2014-2017 and 2020-2022 was 6.618 MJ m^{-2}, corresponding to a 33.6% reduction relative to the reference period mean. Thus, the reported 53.3% value represents the reduction during the 2020-2022 late post transition period rather than the mean reduction across the entire post transition interval. Linear regression using the 11 annual estimates satisfying the ≥10 valid month inclusion criterion, excluding 2009, 2018 and 2019, yielded a statistically significant depletion rate of -562 kJ m^{-2} yr^{-1} (R^2 = 0.57, p = 0.007). As a sensitivity test, the regression was repeated using only the nine years containing all 12 monthly means. This analysis produced a depletion rate of -586 kJ m^{-2} yr^{-1} (R^2 = 0.67, p = 0.007), confirming that the negative trend remained statistically significant after excluding the two 10 month estimates.

Additional robustness tests confirmed that the depletion trend was not controlled solely by the 2011 maximum. The Theil-Sen median slope was -550 kJ m^{-2} yr^{-1} (95% confidence interval: -1020 to -222 kJ m^{-2} yr^{-1}), and the Mann-Kendall test indicated a significant monotonic decline (τ = -0.636, exact p = 0.006). Leave one year out regressions produced slopes ranging from -607 to -422 kJ m^{-2} yr^{-1}, with all trends remaining statistically significant (p = 0.005-0.027). Specifically, excluding the 2011 maximum produced a slope of -422 kJ m^{-2}

458 yr^{-1} (R^2 = 0.57, p = 0.012). The OLS residuals showed negligible first order serial correlation
459 (lag-1 r = -0.002; Durbin-Watson statistic = 1.98).



460 **Figure 7.** Internal energy diagnostics. (a) Mean conductive heat flux profiles for the pre 2013
461 and post 2013 periods. (b) Mean conductive heat flux divergence profiles. (c) Annual cold
462 content evolution (2009-2022) with linear regression and period means.

463 **4.3 Thermodynamic diagnostics and scale parameters**

464 The calculated thermodynamic diagnostics and scale parameters are summarised in
465 Supplementary Table S9. The annual evolution of the relative energy barrier is presented in
466 Figure 8. The relative energy barrier ranged from 68.7-144.8% during 2009-2013 and from
467 15.7-98.8% from 2014 onwards, with the latter range including the partial 2019 record. When
468 restricted to complete post transition annual records, the range was 39.9-98.8%. The mean
469 value during the 2020-2022 late post transition period was 46.7% of the 2010-2013 reference
470 period mean. By definition, $EB_{relative}$ is directly proportional to annual cold content and
471 therefore follows the same temporal evolution. Using the accumulation rate converted to the
472 ice equivalent velocity (w_{ice} = 0.491 m yr^{-1}), the reference whole column advective Péclet
473 number was 8.0. Under a ±20% accumulation rate sensitivity, this value ranged from 6.4 to
474 9.6. The alternative mean firn density conversion gave Pe_{adv}=11.3, with a corresponding
475 sensitivity range of 9.0-13.6. Because H, b, and α were held constant, Pe_{adv} and τ are fixed
476 contextual scale parameters and were not used to identify a temporal change across the 2013
477 transition.

The idealized full depth conductive timescale was 926 years, substantially longer than the 2009-2022 observation period. This value applies to the assumed 560 m slab and should not be interpreted as the relaxation time of the observed 4-10 m interval.

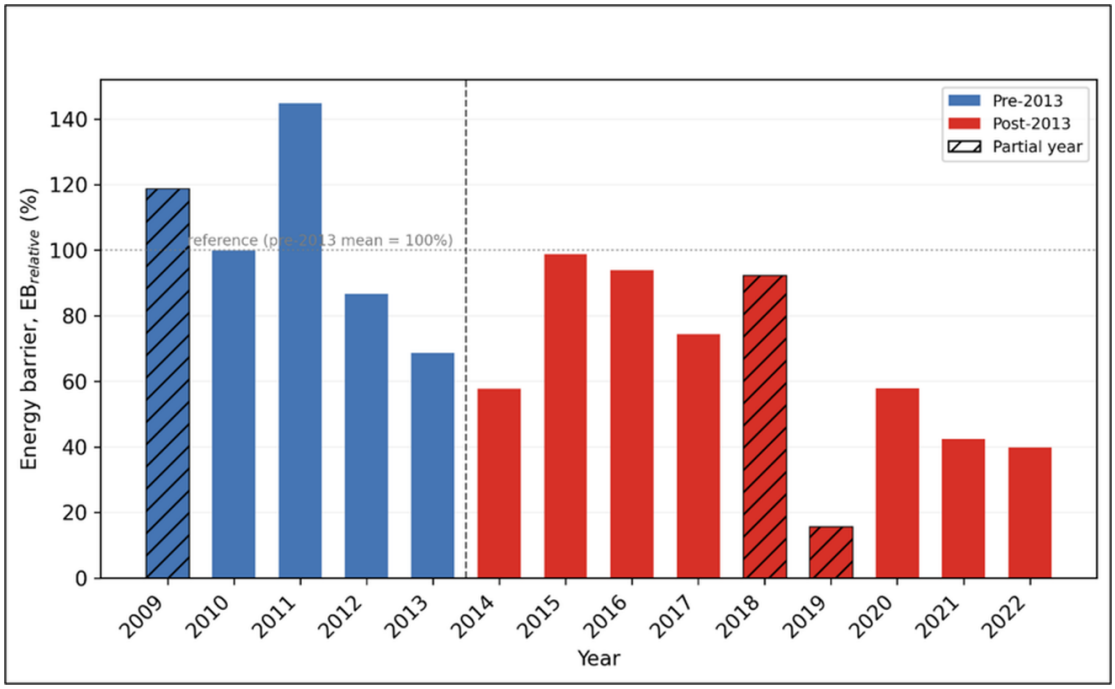


Figure 8. Annual evolution of the relative energy barrier ($EB_{relative}$) for the Austfonna firn column (2009-2022).

4.4 Empirical cold content pathways and climate context

Future cold content was illustrated using two empirical pathways:

1. linear extrapolation of the observed depletion trend and
2. Exponential decay fitted to the observed cold content series. SSP2-4.5 and SSP5-8.5 surface temperature trajectories were retained separately as external climate context and were not propagated into scenario specific cold content projections (IPCC AR6, 2021; Hanssen-Bauer et al., 2019).

4.4.1 Cold content depletion pathways

Projected cold content pathways derived from the observed depletion record are presented in Figure 9, with the corresponding numerical values summarized in Table 2. Both pathways were anchored to the actual 2022 annual cold content of 3.975 MJ m^{-2}. Linear extrapolation using the observed depletion rate of -562 kJ m^{-2} yr^{-1} reaches CC_{col} = 0 in approximately 2029. The exponential projection uses the fitted e-folding time of 12.95 years

and the same 2022 anchor, giving projected cold contents of 2.14 MJ m^{-2} in 2030 and 0.46 MJ m^{-2} in 2050, with 95% depletion relative to the 2022 value occurring in approximately 2061. Projected surface temperature changes under SSP2-4.5 and SSP5-8.5, together with the regional Svalbard annual mean trend of +0.87 °C $decade^{-1}$ during 1971-2017, are summarized in Table 3. This regional trend is distinct from the +1.7 °C $decade^{-1}$ Svalbard Airport trend for 1991-2018 because the spatial coverage and observation periods differ. These trajectories provide external climate context only and were not propagated into scenario specific cold content projections. The observed trend row in Table 3 is a linear extrapolation of the regional 1971-2017 trend over a 28-78 year horizon and, by 2100, exceeds even the SSP5-8.5 projection, it is included as an illustrative upper bound sensitivity check rather than a preferred projection, since real warming trajectories are not expected to remain linear over such periods. The calculated thermal relaxation time (τ = 926 years) exceeds both the duration of the observational record and the empirical projection horizons presented here.

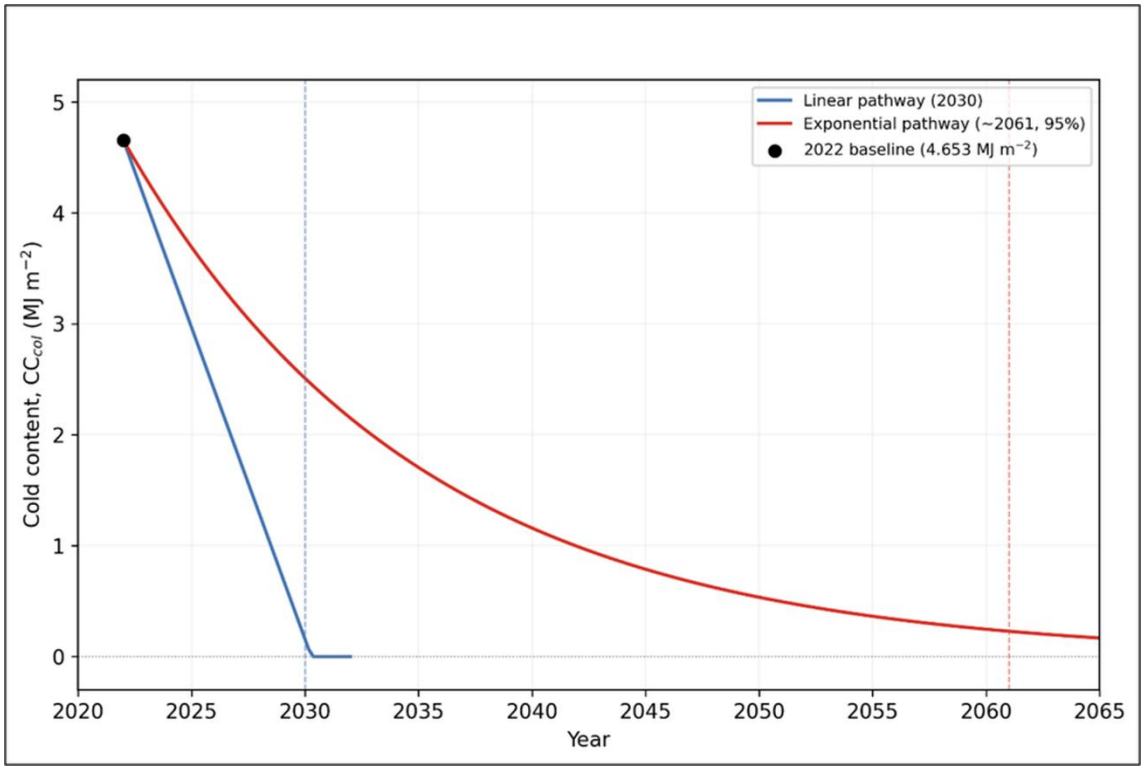


Figure 9. Projected cold content pathways to 2065. The linear pathway reaches zero, whereas the exponential pathway approaches zero asymptotically; 2061 denotes 95% depletion relative to the 2022 anchor.

Table 2. Cold content projection pathways. (Values are rounded to 0.1 MJ m^{-2}. Bracketed values are approximate 95% prediction intervals. Both pathways are anchored to the observed 2022 cold content, and the linear pathway is constrained to $CC_{col} \geq 0$.)

Projection pathway	**Basis**	**Projected CC_{col} at 2030 (MJ m^{-2})**	**Projected CC_{col} at 2050 (MJ m^{-2})**	**Depletion criterion and estimated year**
Linear	2022 CC_{col} = 3.975 MJ m^{-2}; depletion rate = -0.562 MJ m^{-2} yr^{-1}	0.0 [0.0-5.1]	0.0, physical floor	CC_{col}=0: approximately 2029
Exponential	2022 CC_{col} = 3.975 MJ m^{-2}; τCC_{col} = 12.95 yr	2.1 [1.1-4.1]	0.5 [0.1-1.7]	95% depletion relative to the 2022 anchor: approximately 2061

Table 3. Climate change context (not propagated into cold content projections).

Climate context	**Reference period/anchor**	**ΔT by 2050 (°C)**	**ΔT by 2100 (°C)**
SSP2-4.5	1971-2000	+1.5	+3.0
SSP5-8.5	1971-2000	+2.5	+6.0
Regional Svalbard annual mean trend, 1971-2017 (illustrative extrapolation)	2022 projection anchor	+2.4	+6.8

Note: *SSP temperature anomalies are relative to the 1971-2000 reference period. The observed trend row reports temperature change from a 2022 projection anchor. Because the reference periods differ, these values provide climate context only and are not absolute surface temperature projections or inputs to the cold content pathways.*

5. Discussion

5.1 Reinterpreting the 2013 transition

The 2013 cold to temperate transition at Austfonna was first established by (Innanen et al., 2025b) using CryoGrid simulations forced by borehole and firn core observations, who attributed the shift to enhanced meltwater percolation and latent heat release during refreezing. The present analysis complements this interpretation through an observation derived thermodynamic framework based directly on the borehole temperature record. (Innanen et al.,

2025b) report a modelled cold content series for the upper 10 m of firn that shows pronounced interannual variability but no statistically significant long term trend. The borehole derived cold content series calculated here for the 4-10 m interval shows a statistically significant depletion trend of -562 kJ m^{-2} yr^{-1} (R^2 = 0.57, p = 0.007), with cold content decreasing from 9.964 to 4.653 MJ m^{-2} between the defined comparison periods. Direct comparison with the model derived trend reported by Innanen et al. (2025b) is not possible because the two analyses use different vertical windows and calculation methods. The difference in trend significance is therefore not interpreted as disagreement between the studies. Innanen et al. (2025b) established the transition mechanism, whereas the present analysis quantifies temperature derived cold content change within the 4-10 m interval.

This individual transition framing sits within a broader recognition, reviewed by (Irvine-Fynn et al., 2011), that polythermal glacier hydrology and thermal structure have historically been understudied relative to fully temperate systems, despite polythermal regimes being globally common across the Arctic, Svalbard, and parts of the Antarctic periphery. Austfonna's 14-year continuous record is unusual in this context precisely because most site level polythermal thermal studies span at most a few melt seasons.

The depth resolved warming analysis adds a further layer to this reinterpretation. After correction for multiple depth wise comparisons, the all available year analysis retained significant warming at 8-10 m, whereas the complete calendar year sensitivity analysis retained significant warming at 3-10 m. A single "warming trend" description of the 2013 transition, of the kind common in the wider borehole literature (Cuffey and Paterson, 2010), would therefore be misleading if applied uniformly across depth: the near surface firn is dominated by atmospherically driven interannual noise, while the deeper firn precisely the zone sampled by the cold content and energy barrier diagnostics carries the coherent long term signal. Despite these significant trends, the warming rate profile was non monotonic, decreasing toward approximately 7.5-8 m before increasing near 10 m. This pattern should not be interpreted as simple attenuation of surface warming with depth. It may reflect phase lagged forcing, lower boundary effects, changing sensor geometry and interpolation between thermistors. Because adjacent interpolated nodes share sensor observations, they are not statistically independent. The mechanism responsible for the increased warming rate near the lower boundary therefore cannot be identified uniquely from the present analysis.

5.2 Thermal memory and energy barrier: physical meaning

The cold content framework used here draws on an established line of work treating firn cold content as a measure of the latent heat buffering capacity of a glacier or ice sheet column (Vandecrux et al.,2020;Pfeffer and Humphrey, 1996). Vandecrux et al., (2020) demonstrated, across nine Greenland sites over 1998-2017, that cold content is a useful decadal scale diagnostic of firn thermal state but noted that it had generally been treated as an isolated quantity rather than embedded within a broader energy accounting framework precisely the gap this study's linked CC_{col}-$EB_{relative}$-Pe_{adv}-τ cascade is designed to close.

Although $EB_{relative}$ is mathematically proportional to cold content, expressing the result as a relative energy barrier provides an intuitive measure of the remaining thermal resistance relative to the pre transition state. The 5.311 MJ m^{-2} difference between the 2010-2013 and 2020-2022 mean cold content values corresponds to a latent heat equivalent of 15.9 kg m^{-2}, or 15.9 mm w.e., using a latent heat of fusion of 334 kJ kg^{-1}. For scale, this is approximately 3.5% of the stated mean annual accumulation of 0.45 m w.e. This conversion provides an energy equivalent magnitude only and should not be interpreted as a measured refreezing total, because no independent meltwater or refreezing mass budget is available.

5.3 Role of advection in heat transport

Using the full ice thickness of 560 m and the ice equivalent surface accumulation velocity, the reference whole column Pe_{adv} is 8.0, following the classical vertical advection diffusion scaling of Robin (1955) and Cuffey and Paterson (2010). The alternative firn density conversion gives Pe_{adv} =11.3 as a density conversion sensitivity. These values are surface accumulation, whole column scaling parameters and do not quantify depth mean advection or local heat transport within the observed 4-10 m interval. Mechanical rescaling to characteristic lengths of 10 m and 6 m produces substantially smaller values, demonstrating the strong dependence of Pe_{adv} on the selected length scale. The calculation therefore indicates that vertical advection may be relevant at the whole column scale, but it does not establish advection dominance or a temporal change in heat transfer regime within the observed firn interval.

5.4 Interpretation of the full depth conductive timescale

The calculated τ =926 years represents the fundamental conductive timescale of an idealized 560 m slab under the stated diffusivity and boundary assumptions. It was not inferred from temporal adjustment in the borehole record and does not describe the relaxation of the observed 4-10 m interval. Applying the same equation to characteristic lengths of 10 m and 6 m gives scale estimates of approximately 0.30 and 0.11 years, respectively. These shorter values are also idealized because the calculation excludes vertical advection, latent heat effects, evolving thermal properties, and changing boundary forcing. The 926 year value therefore indicates that purely conductive adjustment across the full ice thickness can be slow, but it does not demonstrate that the observed firn is committed to multi century evolution regardless of future climate forcing.

5.5 Scope of the thermodynamic framework

Traditional borehole analyses commonly report temperature, warming rate, and zero curtain duration. The present framework complements these measures by expressing the observed thermal state as cold content and its normalized relative energy barrier, while Pe_{adv} and τ provide scale dependent contextual parameters under the prescribed site assumptions.

This provides three practical advantages. First, thermal state is quantified using physically interpretable quantities, including thermal memory (MJ m^{-2}) and characteristic relaxation time (years), rather than temperature trends alone. Second, CC_{col}, $EB_{relative}$ are calculated consistently and can be compared between periods. In contrast, Pe_{adv} and τ provide site scale context and remain unchanged between periods unless the prescribed values of H, b, or α are updated. Comparisons between sites therefore require consistent parameter definitions and characteristic length scales. Third, the framework requires a borehole temperature record, a representative density profile, an accumulation rate estimate, an ice thickness estimate, and a reference thermal diffusivity, making comparable analyses feasible for other polythermal ice masses without requiring a fully coupled energy balance model at every location.

5.6 A generalised workflow

This study also highlights a practical methodological lesson for future thermodynamic analyses of glacier boreholes. Any derived thermal transport quantity that combines a velocity

or flux term with a characteristic length scale should explicitly define and physically justify that length scale before computation. During development of the present framework, a candidate latent heat analogue to Pe_{adv} was evaluated but found to vary by almost two orders of magnitude depending on the assumed characteristic length scale. This instability resulted from combining a near surface diagnostic window with the full ice thickness by analogy with the advective Péclet number. Explicit justification of characteristic length scales at the formulation stage is therefore recommended when extending the framework to other sites. Uncertainty analysis and limitations of this study are provided in Supplementary Section S1 and S2 respectively.

6. Conclusion

This study applied a linked thermodynamic diagnostic framework to the Austfonna borehole record. CC_{col} and $EB_{relative}$ describe the same temperature derived thermal state on absolute and normalized scales, whereas Pe_{adv} and τ provide fixed site scale context under the prescribed parameters. Depth resolved warming significance depended on seasonal coverage. After correction for multiple comparisons, significant trends were retained at 8-10 m using all available annual estimates and at 3-10 m using complete calendar year records. Mean cold content during 2020-2022 was 53.3% lower than the 2010-2013 reference period mean, while the mean across all retained post transition annual estimates was 33.6% lower. The relative energy barrier during 2020-2022 was correspondingly 46.7% of its reference value. Together with the independently established 2013 transition, the significant long term cold content trend indicates sustained thermodynamic evolution following the transition. These diagnostics quantify the magnitude of that evolution but do not independently identify 2013 as a statistical breakpoint. The framework's input requirements a borehole temperature record, a representative density profile, an accumulation rate estimate, an ice thickness estimate, and a reference thermal diffusivity make it substantially less demanding than fully coupled energy balance models and broadly transferable to other polythermal settings, though full validation across a wider sample of ice masses remains for future work. The 926 year value is an idealized full depth conductive timescale rather than a relaxation time measured within the 4-10 m firn interval. It provides context for potentially slow conductive adjustment across the full ice thickness but does not independently establish climate invariant multi century thermal commitment. The results therefore distinguish rapid changes in shallow cold content from the much longer theoretical diffusion scale of the full ice column.

Acknowledgement

The authors gratefully acknowledge the continued encouragement and dedicated support of our Director and the Sri Sringeri Sharada Peetham, Sringeri, whose unwavering commitment to scientific research and polar science has been instrumental in enabling this work. The authors further acknowledge the support rendered by Prazim Trading and Investment Company Private Limited (PTICL) and Tarish Investment and Trading Company Limited (TITCL) toward the successful completion of this research. The authors also acknowledge the scientific community, data centres, and international agencies that maintain and freely provide high quality observational, reanalysis, and geospatial datasets, without which studies of remote polar environments would not be possible. The authors gratefully acknowledge the Norwegian Polar Institute and the Norwegian Polar Data Centre (NPDC) for providing open access to the Austfonna observational dataset used in this study, which greatly facilitated the analysis and interpretation of the thermal evolution of the ice cap. The Norwegian Polar Data Centre provides free and open access to valuable scientific datasets from the Arctic and Antarctic, supporting reproducible polar research worldwide.

Declaration of Generative AI and AI assisted technologies in the writing process:

During the preparation of this manuscript, the authors used AI assisted language tools to improve the clarity and readability of the text. All scientific content, analyses, interpretations, and conclusions were developed and verified by the authors. The authors carefully reviewed and edited all AI assisted outputs and accept full responsibility for the content of the published work.

Data Availability Statement:

The borehole temperature data (2009-2022) from the three thermistor strings, together with the corresponding CryoGrid-modelled surface heights used to track sensor depths, are archived at the Norwegian Polar Institute (NPOLAR) data centre and available at https://doi.org/10.21334/NPOLAR.2025.10DB6623.

Competing interest:

All the authors declare they have no conflict of interest.

References

Benn, D. I., & Evans, D. J. A. (2010). *Glaciers and glaciation* (2nd ed.). Routledge. https://doi.org/10.4324/9780203785010

Calonne, N., Flin, F., Morin, S., Lesaffre, B., Rolland du Roscoat, S., & Geindreau, C. (2011). Numerical and experimental investigations of the effective thermal conductivity of snow. *Geophysical Research Letters, 38*(23), L23501. https://doi.org/10.1029/2011GL049234

Carslaw, H. S., & Jaeger, J. C. (1959). *Conduction of heat in solids* (2nd ed.). Clarendon Press.

Contribution of Working Group I. (2021). Climate Change 2021: The Physical Science Basis.

Cuffey, K. M., & Paterson, W. S. B. (2010). *The physics of glaciers* (4th ed.). Academic Press.

Dowdeswell, J. A., Drewry, D. J., Cooper, A. P. R., Gorman, M. R., Liestøl, O., & Orheim, O. (1986). Digital mapping of the Nordaustlandet ice caps from airborne geophysical investigations. *Annals of Glaciology, 8*, 51–58. https://doi.org/10.3189/S0260305500001130

Hanssen-Bauer, I., Førland, E. J., Hisdal, H., Mayer, S., Sandø, A. B., & Sorteberg, A. (Eds.). (2019). *Climate in Svalbard 2100: A knowledge base for climate adaptation*. Norwegian Centre for Climate Services, NCCS Report 1/2019.

Innanen, S., Vikhamar Schuler, T., & Moholdt, G. (2025a). *Firn temperature data from Austfonna, Svalbard, 2009-2022* [Data set]. Norwegian Polar Institute. https://doi.org/10.21334/NPOLAR.2025.10DB6623

Innanen, S., Hock, R., Schmidt, L. S., Schuler, T. V., Covi, F., & Moholdt, G. (2025b). Witnessing the transition from cold to temperate firn on Austfonna ice cap, Svalbard, through observations and model simulations. *Journal of Glaciology, 71*, Article e101. https://doi.org/10.1017/jog.2025.10072

Irvine-Fynn, T. D. L., Hodson, A. J., Moorman, B. J., Vatne, G., & Hubbard, A. L. (2011). Polythermal glacier hydrology: A review. *Reviews of Geophysics, 49*(4). https://doi.org/10.1029/2010RG000350

Nordli, Ø., Wyszyński, P., Gjelten, H. M., Isaksen, K., Łupikasza, E., Niedźwiedź, T., & Przybylak, R. (2020). Revisiting the extended Svalbard Airport monthly temperature series, and the compiled corresponding daily series 1898–2018. *Polar Research, 39*, Article 3614. https://doi.org/10.33265/polar.v39.3614

Pfeffer, W. T., & Humphrey, N. F. (1996). Determination of timing and location of water

movement and ice-layer formation by temperature measurements in sub-freezing snow. *Journal of Glaciology, 42*(141), 292-304. https://doi.org/10.3189/S0022143000004159

Robin, G. de Q. (1955). Ice movements and temperature distribution in glaciers and ice sheets. *Journal of Glaciology, 2*(18), 523-532. https://doi.org/10.3189/S0022143000017885

Schmidt, L. S., Schuler, T. V., Thomas, E. E., & Westermann, S. (2023). Meltwater runoff and glacier mass balance in the high Arctic: 1991–2022 simulations for Svalbard. *The Cryosphere, 17*(7), 2941-2963. https://doi.org/10.5194/tc-17-2941-2023

Schuler, T. V., Dunse, T., Østby, T. I., & Hagen, J. O. (2014). Meteorological conditions on an Arctic ice cap-8 years of automatic weather station data from Austfonna, Svalbard. *International Journal of Climatology, 34*(6), 2047-2058. https://doi.org/10.1002/joc.3821

Taurisano, A., Schuler, T. V., Hagen, J. O., Eiken, T., Loe, E., Melvold, K., & Kohler, J. (2007). The distribution of snow accumulation across the Austfonna ice cap, Svalbard: Direct measurements and modelling. *Polar Research, 26*, 7-13. https://doi.org/10.1111/j.1751-8369.2007.00004.x

Vandecrux, B., Fausto, R. S., Van As, D., Colgan, W., Langen, P. L., Haubner, K., Ingeman-Nielsen, T., Heilig, A., Stevens, C. M., MacFerrin, M., Niwano, M., Steffen, K., & Box, J. E. (2020). Firn cold content evolution at nine sites on the Greenland ice sheet between 1998 and 2017. *Journal of Glaciology, 66*(258), 591-602. https://doi.org/10.1017/jog.2020.30

Westermann, S., Ingeman-Nielsen, T., Scheer, J., Aalstad, K., Aga, J., Chaudhary, N., Etzelmüller, B., Filhol, S., Kääb, A., Renette, C., Schmidt, L. S., Schuler, T. V., Zweigel, R. B., Martin, L., Morard, S., Ben-Asher, M., Angelopoulos, M., Boike, J., Groenke, B., … Langer, M. (2023). The CryoGrid community model (version 1.0): A multi-physics toolbox for climate-driven simulations in the terrestrial cryosphere. *Geoscientific Model Development, 16*, 2607–2647. https://doi.org/10.5194/gmd-16-2607-2023

Supplementary material

A Thermodynamic Framework for Quantifying Firn Thermal Evolution: Cold Content Depletion, Energy Barrier Reduction and Thermal Commitment of Austfonna Ice Cap, Svalbard (2009-2022)

Geetha Priya M*, Adithya Sunil

Centre for Incubation, Innovation, Research and Consultancy, Jyothy Institute of Technology, Bengaluru-560082.

*geetha.sri82@gmail.com

Deployment	Install date	Sensors	Initial depth range (m below surface)	Logger	Accuracy	End date
T1 string	2009-05-06	10 (T1-T10)	0 to -13.0	Geoprecision M-Log1 A	±0.2°C, resolution 0.01°C	2014-04-29
T2 string	2014-05-03	10 (T1-T10)	+1.0 to -11.0	M-Log5W TNode A50457	±0.1°C (−5 to +50°C)	2015-05-02
T3 string	2015-05-03	10 (T1-T10)	+1.3 to -11.2	M-Log5W TNode (reused)	±0.1°C, resolution 0.01°C	2018-08-27; resumed 2019-04-27 through 2022-12-31

Supplementary Table S1. Borehole metadata

Note: T1 String ended on 29 April 2014 and T2 String began on 3 May 2014. No thermistor observations were available from 30 April to 2 May 2014.

777 **Supplementary Table S2.** Quality control and correction procedures applied before
778 importing the Austfonna borehole temperature observations into the input workbook. The
779 workflow follows the processing instructions accompanying the source dataset.

Rule	Procedure	Correction applied
R1	Thermistor depth reconstruction	Thermistor depths were calculated relative to the CryoGrid simulated surface and reset using the documented installation depths. One physically implausible CryoGrid surface height value of 18.899 m was replaced by linear interpolation with 4.731 m before recalculating sensor depths.
R2	Above surface thermistors	Observations were removed whenever a thermistor was positioned above the modelled firn surface.
R3	Air temperature contamination	Observations displaying atmospheric variability rather than subsurface firn temperature behaviour were removed. This included affected upper sensors of String 3 until approximately mid 2016.
R4	Post installation disturbance	Approximately two months of observations following each thermistor string installation were removed.
R5	Sensor zero offset correction	Each sensor was evaluated using stable melt season temperature plateaus. Where the absolute zero offset exceeded 0.1 °C, the affected observations were shifted using the estimated sensor specific bias. Corrected values exceeding 0 °C were constrained to 0 °C.

780

781 **Supplementary Table S3.** Physical constants

Symbol	Parameter	Value	Unit	Source
k_{ice}	Thermal conductivity, pure ice	2.09	W m^{-1} K^{-1}	Cuffey and Paterson (2010)
c	Specific heat capacity, ice	2097	J kg^{-1} K^{-1}	Cuffey and Paterson (2010)
ρ_{ice}	Density, pure ice	917	kg m^{-3}	Cuffey and Paterson (2010)
T_f	Melting point	0	°C	-
α	Thermal diffusivity, pure ice (reference)	1.087×10^{-6}	m^2 s^{-1}	Derived: $k_{ice}/(\rho_{ice} \cdot c)$
$k_{firn}(\rho)$	Firn thermal conductivity (depth varying)	$0.024 - 1.23\times10^{-4}\cdot\rho + 2.5\times10^{-6}\cdot\rho^2$	W m^{-1} K^{-1}	Calonne et al., (2011)
H	Ice thickness at dome (used as proxy for borehole site)	560	m	Dowdeswell et al., (1986); Schuler et al., (2014)
b	Accumulation rate, summit	0.45	m w.e. yr^{-1}	Taurisano et al., (2007); Schuler et al., (2014)
$\rho_{firn\ mean}$	Mean firn density (accumulation conversion)	650	kg m^{-3}	Reference density profile
-	Primary cold content integration window	4.0-10.0	m	Analysis scope decision
w_{ice}	Surface accumulation converted to ice equivalent velocity ($b_{\rho w}$ / ρ_{ice})	0.491	m yr^{-1}	Derived from b, ρ_w, and ρ_{ice}; Cuffey & Paterson (2010)
w_{firn}	Near surface firn burial velocity ($b_{\rho w}$ / $\rho_{firn,mean}$)	0.692	m yr^{-1}	Derived using assumed mean firn density (650 kg m^{-3}); density conversion sensitivity

782 **Supplementary Table S4.** Thermodynamic state variable definitions

Variable	Symbol	Equation	Unit	Physical interpretation
Cold content	CC_{col}	$\int \rho(z) \cdot c \cdot (T_f - T(z)) dz$, $T(z) < 0$, integrated 4.0-10.0 m	MJ m^{-2}	Thermal memory: energy required to warm the analysed firn column to the melting point before additional energy can contribute to melting.
Energy barrier	$EB_{relative}$	(CC_{col}(period) / CC_{col}(reference period)) × 100	dimensionless (%)	Relative resistance remaining to full temperate transition, expressed against a defined reference period
Thermal relaxation time	τ	$H^2/(\pi^2 \cdot \alpha)$	years	Idealized fundamental conductive timescale for a 560 m slab with prescribed temperature boundary perturbations. The numerical coefficient depends on the boundary conditions; this value is not the relaxation time of the observed 4-10 m interval.
Advective Péclet number	Pe_{adv}	wL/α_{ice}	Dimensionless	Scale dependent ratio of vertical advection to thermal diffusion. The reported whole column values use L=H=560 m. Values obtained using L=10 m or 6 m are length scale sensitivity illustrations and not locally calibrated estimates.

783

784

785

Supplementary Table S5a. Depth resolved warming trend statistics (2009-2022) (P values were adjusted separately for each analysis using the Benjamini-Hochberg false discovery rate procedure; $q < 0.05$ was considered significant.)

Depth (m)	Trend (°C decade^{-1})	R^2	p value	False Discovery Rate (FDR) adjusted q value	Significant after FDR correction (q < 0.05)
0.5	+1.009	0.066	0.419	0.5039	No
1.0	+0.717	0.049	0.470	0.5217	No
1.5	+0.205	0.004	0.832	0.8316	No
2.0	+0.294	0.010	0.730	0.7685	No
2.5	+0.532	0.053	0.428	0.5039	No
3.0	+0.658	0.109	0.250	0.3335	No
3.5	+0.696	0.161	0.155	0.2220	No
4.0	+0.710	0.222	0.089	0.1370	No
4.5	+0.682	0.283	0.050	0.0840	No
5.0	+0.623	0.328	0.032	0.0632	No
5.5	+0.541	0.342	0.028	0.0632	No
6.0	+0.479	0.352	0.025	0.0632	No
6.5	+0.417	0.321	0.035	0.0632	No
7.0	+0.388	0.332	0.031	0.0632	No
7.5	+0.380	0.359	0.024	0.0632	No
8.0	+0.429	0.423	0.012	0.0470	Yes
8.5	+0.527	0.477	0.006	0.0314	Yes
9.0	+0.639	0.506	0.004	0.0287	Yes
9.5	+0.769	0.546	0.003	0.0252	Yes
10.0	+0.889	0.596	0.001	0.0244	Yes

790 **Supplementary Table S5b.** Sensitivity analysis using complete calendar year temperature
791 records only. (P values were adjusted separately for each analysis using the Benjamini-
792 Hochberg false discovery rate procedure; $q < 0.05$ was considered significant.)

Depth (m)	n	Trend (°C decade^{-1})	R^2	P value	FDR adjusted q value	Significant after FDR correction (q < 0.05)
0.5	7	+2.448	0.444	0.102	0.1201	No
1.0	8	+1.732	0.455	0.067	0.0832	No
1.5	9	+0.771	0.066	0.504	0.5039	No
2.0	9	+0.825	0.101	0.404	0.4250	No
2.5	9	+1.055	0.303	0.125	0.1389	No
3.0	9	+1.168	0.544	0.023	0.0387	Yes
3.5	9	+1.128	0.616	0.012	0.0349	Yes
4.0	9	+1.070	0.658	0.008	0.0349	Yes
4.5	9	+0.961	0.660	0.008	0.0349	Yes
5.0	9	+0.838	0.655	0.008	0.0349	Yes
5.5	9	+0.704	0.631	0.011	0.0349	Yes
6.0	9	+0.606	0.624	0.011	0.0349	Yes
6.5	9	+0.517	0.577	0.018	0.0382	Yes
7.0	9	+0.426	0.521	0.028	0.0404	Yes
7.5	9	+0.334	0.485	0.037	0.0496	Yes
8.0	9	+0.320	0.603	0.014	0.0349	Yes
8.5	9	+0.374	0.566	0.019	0.0382	Yes
9.0	9	+0.446	0.523	0.028	0.0404	Yes
9.5	9	+0.547	0.556	0.021	0.0382	Yes
10.0	9	+0.671	0.622	0.012	0.0349	Yes

793

794 **Supplementary Table S6.** Annual minimum temperature profile (ΔT was not calculated for
795 2012 and 2013 because the annual mean temperature at 0.5 m was unavailable).

Year	T_min (°C)	Depth of T_min (m)	ΔT (0.5-10.0 m, °C)
2009	-1.722	0.5	-0.05
2010	-5.105	0.5	-4.08
2011	-5.363	0.5	-4.28
2012	-3.882	1.0	N/A[1]
2013	-1.805	3.0	N/A[1]
2014	-2.181	0.5	-2.11
2015	-3.275	0.5	-2.86
2016	-3.164	2.0	-1.03
2017	-4.997	0.5	-4.83
2018	-5.495	0.5	-5.21
2019	-1.148	0.5	-1.09
2020	-3.714	0.5	-3.55
2021	-2.841	0.5	-2.73
2022	-2.156	1.0	-1.18

Supplementary Table S7. Annual zero curtain duration at 4.0 m and maximum annual depth of the 0 °C isotherm (2009-2022).

Year	Zero curtain duration at 4.0 m (days)	Maximum 0 °C isotherm depth (m)	Classification	Data completeness
2009	73	7.0	Pre transition	Partial
2010	83	7.5	Pre transition	Complete
2011	30	8.5	Pre transition	Complete
2012	91	9.5	Pre transition	Complete
2013	100	2.5	Transition year	Complete
2014	94	10.0	Post transition	Partial
2015	102	10.0	Post transition	Partial
2016	146	10.0	Post transition	Complete
2017	71	10.0	Post transition	Complete
2018	0	10.0	Post transition	Partial
2019	122	10.0	Post transition	Partial
2020	138	10.0	Post transition	Complete
2021	114	10.0	Post transition	Complete
2022	119	10.0	Post transition	Complete

Remark: *Record for 2018 ends 27 August ahead of the 8 month logger gap; the zero curtain value reflects incomplete seasonal coverage, not the absence of zero curtain activity. Zero curtain duration was calculated using $|T| \leq 0.05$ °C, whereas maximum 0 °C isotherm depth was defined as the deepest grid node at which $T \geq 0$ °C occurred on at least one valid day. A value of 10.0 m indicates that the isotherm reached the lower boundary of the analysis grid; its actual maximum depth may exceed 10 m. Records for 2009, 2014, 2015, 2018 and 2019 were incomplete and were retained for descriptive annual presentation only; they were excluded from the complete calendar year period mean comparison.*

Supplementary Table S8. Annual cold content series for the Austfonna firn column (2009-2022).

Year	Cold content, CC_{col} (MJ m^{-2})	Valid months	Record status	Analysis period
2009	11.836	6	Partial (Jul-Dec)	Excluded from trend
2010	9.957	12	Complete	Pre 2013
2011	14.424	12	Complete	Pre 2013
2012	8.629	12	Complete	Pre 2013
2013	6.847	12	Complete	Pre 2013
2014	5.752	10	Retained (10 months; May-Jun missing)	Post 2013
2015	9.843	10	Retained (10 months; May-Jun missing)	Post 2013
2016	9.359	12	Complete	Post 2013
2017	7.414	12	Complete	Post 2013
2018	9.199	8	Partial (Jan-Aug)	Excluded from trend
2019	1.565	6	Partial (Jul-Dec)	Excluded from trend
2020	5.763	12	Complete	Post 2013
2021	4.221	12	Complete	Post 2013
2022	3.975	12	Complete	Post 2013

Remark: 1- The month ranges in the record status column refer to months satisfying the annual cold content inclusion requirement of at least 15 valid daily 4-10 m profiles. Although observations began in May 2009 and resumed in April 2019, the accepted monthly means in both partial years extend from July to December following installation/restart disturbance removal and depth coverage screening.

2- Annual cold content estimates were retained when at least 10 monthly means were available. Accordingly, 2014 and 2015 were included in the primary regression despite missing May and June. They are classified as retained incomplete year estimates rather than complete calendar year records. As a sensitivity test, the regression was repeated using only the nine years containing all 12 monthly means. The resulting depletion rate was -586 kJ m^{-2} yr^{-1} (R^2 = 0.67,

822 *p = 0.007), confirming that the negative trend remained statistically significant after excluding*
823 *the two 10 month estimates.*

824

825

826

827

828

Supplementary Table S9. Summary of thermodynamic diagnostics and scale parameters. Analytical and Monte Carlo uncertainty estimates for CC_{col}, $EB_{relative}$, Pe_{adv},firn and τ are reported in Supplementary Section S1; the ranges shown for Pe_{adv} are deterministic accumulation rate sensitivities.

Variable	Symbol	Value	Units	Remarks
Mean pre 2013 cold content	$\mathbf{CC_{col}}$	9.964	MJ m^{-2}	Reference period (2010-2013)
Mean post 2013 cold content	$\mathbf{CC_{col}}$	4.653	MJ m^{-2}	Mean of 2020-2022
Cold content reduction	$\mathbf{\Delta CC_{col}}$	53.3	%	Relative to pre 2013 mean
Relative energy barrier	$\mathbf{EB_{relative}}$	46.7	%	Directly proportional to annual cold content
Thermal relaxation time	$\boldsymbol{\tau}$	926	yr	Idealized full depth conductive scale for H=560 m; not an observed 4-10 m firn relaxation time.
Reference whole column Péclet number	$\mathbf{Pe_{adv}}$	8.0	-	Ice equivalent whole column scaling; deterministic ±20% accumulation rate sensitivity: 6.4-9.6
Firn density sensitivity	$\mathbf{Pe_{adv,firn}}$	11.3	-	Mean firn density scaling; 9.0-13.6 for ±20% accumulation

S1. Uncertainty analysis and uncertainty propagation

Uncertainty propagation was performed using root sum square combination through the complete calculation chain.

The analysis incorporated:

- thermistor accuracy (±0.1-0.2°C, depending on deployment),
- interpolation uncertainty associated with the 0.5 m vertical grid,
- firn density uncertainty (±5%),
- accumulation rate uncertainty (±20%),
- ice thickness uncertainty (±5%),
- pure ice reference thermal diffusivity uncertainty (±10%).

These uncertainties were propagated to cold content, the relative energy barrier, the firn density Péclet number sensitivity, and the thermal relaxation time. The corresponding analytical and Monte Carlo uncertainty results are reported below.

Uncertainty was propagated through the complete calculation chain using two independent methods: (i) root sum square (RSS) analytical first order propagation through each governing equation, and (ii) Monte Carlo simulation (200,000 samples, Gaussian distributed inputs) as a cross check for the more strongly nonlinear quantities. For cold content, temperature uncertainty at each interpolated depth node was propagated through the trapezoidal integration used to compute the 4.0-10.0 m column cold content. For the thermodynamic state variables ($EB_{relative}$, Pe_{adv}, and τ), both RSS and Monte Carlo propagation were applied to the governing equations, with results compared directly.

S1.1 Input uncertainties

The uncertainty sources adopted in this study are summarised in Supplementary Table S10.

Supplementary Table S10. Input uncertainties used for uncertainty propagation.

Source	Uncertainty Scale	Basis
Sensor accuracy (2009-05-06 to 2014-04-29)	±0.20°C	Manufacturer specification
Sensor accuracy (2014-05-03 to 2022-12-31)	±0.10°C	Manufacturer specification

Vertical interpolation	±0.04°C	Estimated from local temperature gradient (~0.15°C m^{-1}) × half grid spacing (0.25 m)
Firn density	±5%	Representative uncertainty adopted for the reference density profile
Accumulation rate	±20%	Adopted sensitivity scale; not an empirically determined standard uncertainty.
Ice thickness	±5%	
Pure ice reference thermal diffusivity	±10%	

S1.2 Cold content uncertainty

Temperature and interpolation uncertainties were combined at each of the thirteen 0.5 m grid nodes and propagated using trapezoidal weights of 0.25 m at the endpoints and 0.50 m at the interior nodes. Assuming independent node errors and a single 5% multiplicative density uncertainty shared across depths and periods:

$$uCC = \sqrt{[(\rho_{mean} \times c \times uT)^2 \times \Sigma ai^2 + (0.05 \times CC)^2]} \quad \text{(S1)}$$

Where, $\Sigma ai^2 = 2.875\ m^2$, $\rho_{mean} = 820\ kg\ m^{-3}$, and uT = 0.204 °C and 0.108 °C for the reference and late periods, respectively. This gives $CC_{reference} = 9.964 \pm 0.78\ MJ\ m^{-2}$ (7.8%) and $CC_{late} = 4.653 \pm 0.39\ MJ\ m^{-2}$ (8.4%). The Monte Carlo results agreed closely. These are first order RSS estimates; a separate common mode sensor offset component was not included.

As a fully correlated calibration offset sensitivity, a uniform temperature shift equal to the manufacturer accuracy would change cold content by approximately ±2.06 MJ m^{-2} for the 2010-2013 reference period (±0.20 °C) and ±1.03 MJ m^{-2} for the 2020-2022 late period (±0.10 °C). These values are sensitivity bounds and were not combined with the random error RSS estimates.

Note: ρ_{mean} = 820 kg m^{-3} is the reference profile mean over the 4.0-10.0 m cold content integration window specifically, distinct from the 650 kg m^{-3} bulk mean used for the advective velocity calculation the difference reflects greater firn compaction at this depth relative to the shallower firn captured in the whole column mean.

S1.3 Relative energy barrier

$EB_{relative} = CC_{late}/CC_{reference} \times 100 = 4.653/9.964 \times 100 = 46.7\%$. The same reference density profile was used for both periods. Density uncertainty was therefore represented as a common multiplicative component in the numerator and denominator and cancels in the ratio. Let $u_{reference} = 7.8\%$, $u_{late} = 8.4\%$, and $u_\rho = 5.0\%$. Accounting for the covariance introduced by the shared density component gives

$$u_{EB} = \sqrt{u_{late}^2 + u_{reference}^2 - 2u_\rho^2} = \sqrt{8.4^2 + 7.8^2 - 2(5.0^2)} = 9.0\% \quad \text{(S2)}$$

Therefore,

$$EB_{relative} = 46.7 \pm 4.2\ percentage\ points$$

Treating the two total cold content uncertainties as independent would give 11.5%; that calculation would be inappropriate under the stated shared density model. The Monte Carlo cross check used the same density draw in the numerator and denominator and produced a mean of 46.9% with an SD of 4.24 percentage points (9.1%).

S1.4 Advective Péclet number

For Pe_{adv}= wH/α, analytical RSS propagation gives:

$$\frac{\delta Pe}{Pe} = \sqrt{\left[\left(\frac{\delta b}{b}\right)^2 + \left(\frac{\delta \rho_{firn}}{\rho_{firn}}\right)^2 + \left(\frac{\delta H}{H}\right)^2 + \left(\frac{\delta \alpha}{\alpha}\right)^2\right]} = 23.5\% \quad \text{(S3)}$$

Pe_{adv}= 11.3± 2.7(implied symmetric range: 8.6-14.0), In this calculation, α = α_{ice}, the pure ice reference diffusivity. Firn density enters only through the alternative burial velocity conversion w_{firn}= $b_{\rho w}/\rho_{firn}$ used for the Pe_{adv} =11.3 sensitivity estimate; it is not used to calculate α_{ice}.

Monte Carlo cross check (200,000 samples): mean = 11.45, SD = 2.72 (23.7%). The distribution was right skewed because Peadv is a product or quotient of several multiplicatively uncertain terms. The Monte Carlo 95% percentile interval was Pe_{adv} = [6.57, 17.26].

This is both wider and asymmetric relative to the analytical symmetric range the symmetric RSS estimate understates the upper tail. The Monte Carlo interval is recommended as the more defensible reported range for Pe_{adv}, given its combined relative uncertainty (23.5%) is large enough that first order linearisation is no longer a close approximation**.**

S1.5 Thermal relaxation time

For $\tau = H^2/\pi^2\alpha$, analytical RSS propagation gives:

$$\frac{\delta \tau}{\tau} = \sqrt{\left[\left(2 \cdot \frac{\delta H}{H}\right)^2 + \left(\frac{\delta \alpha}{\alpha}\right)^2\right]} = 14.1\% \quad \text{(S4)}$$

Here, τ = 926 ± 131 years (implied symmetric range: 795-1057), α = α_{ice}, consistent with the pure ice reference diffusivity used in the reported full depth timescale.

Monte Carlo cross check: mean = 937.7 yr, SD = 134.9 yr (14.4%). The distribution was right-skewed owing to the H^2 term and the multiplicative α dependence. The Monte Carlo 95% percentile interval was τ = [705.5, 1232.7] years (Supplementary Table S11).

As with Pe_{adv}, this interval is recommended over the symmetric RSS range for reporting purposes.

Supplementary Table S11. Propagated uncertainties analytical (RSS) vs. Monte Carlo

Quantity	Value	RSS (symmetric ±)	Monte Carlo mean ± SD	MC 95% Percentile interval	Recommended
Cold content (pre 2013)	9.964 MJ m^{-2}	±0.78 (7.8%)	9.965 ± 0.778 MJ m^{-2} (7.8%)	-	Analytical RSS (first order)
Cold content (post 2013)	4.653 MJ m^{-2}	±0.39 (8.4%)	6.654 ± 0.391 MJ m^{-2} (8.4%)	-	Analytical RSS (first order)
Relative energy barrier	46.7%	±4.2 pp (9.0%)	46.9 ± 4.24 MJ m^{-2} percentage points (9.1%)	-	Analytical covariance model
Firn density Péclet number sensitivity	11.3	±2.7 (23.5%)	11.45 ± 2.72 (23.7%)	[6.57, 17.26]	Monte Carlo Percentile interval
Thermal relaxation time	926 yr	±131 yr (14.1%)	937.7 ± 134.9 yr (14.4%)	[705.5, 1232.7]yr	Monte Carlo Percentile interval

S1.6 Monte Carlo methodology

200,000 samples were drawn per quantity. Inputs were treated as independent Gaussian random variables with mean 1.0 (multiplicative form) or the stated baseline value (additive form for per node temperature errors), with standard deviation equal to the uncertainty listed in Supplementary Table S10. For cold content, per node temperature errors were drawn independently across the thirteen 4.0-10.0 m grid nodes and combined through the trapezoidal integration weights; density uncertainty was drawn once per sample and applied identically to both the pre and post 2013 cold content calculation within that sample, reflecting the use of a single reference density profile for the whole record. For $EB_{relative}$, the same correlated density draw was used for numerator and denominator within each sample, causing density uncertainty to cancel in the ratio, consistent with the analytical treatment. For the firn density Pe_{adv} =11.3 sensitivity estimate, independent multiplicative factors were applied to accumulation rate, firn density used in w_{firn}, ice thickness, and the pure ice reference diffusivity $\alpha = \alpha_{ice}$. For τ, factors were applied only to ice thickness and $\alpha = \alpha_{ice}$. No k_{firn}/ρ combination was used to construct the diffusivity in either calculation.

S2. Limitations

Seven limitations should be recognised.

1. The reference density profile is represented by a single temporally invariant firn core profile rather than repeated density measurements. Consequently, temporal densification caused by compaction or refreezing is not represented.
2. A candidate latent heat Péclet type quantity was evaluated during framework development but was found to be structurally underdetermined owing to ambiguity in the appropriate characteristic length scale. Consequently, it is excluded from the quantitative analysis.
3. The study is based on observations from a single borehole on one Arctic ice cap. Broader validation across multiple polythermal sites remains necessary.
4. The eight month logger gap during 2018, together with other partial year records, reduced the effective sample size available for annual trend analyses.
5. Surface elevation used to track sensor depths was obtained from CryoGrid simulations rather than direct field measurements. Independent uncertainty estimates for the simulated surface heights were unavailable and were therefore not propagated into the depth dependent temperature or cold content uncertainties.
6. The 10 m lower boundary of the interpolated analysis grid limits identification of the maximum depth reached by the 0°C isotherm after 2014.
7. All thermodynamic diagnostics assume laterally homogeneous firn properties at the borehole site. A single vertical borehole cannot resolve lateral variations in density, ice layer distribution, meltwater routing, or preferential flow pathways beyond the immediate borehole vicinity. Although this assumption is common to most borehole based thermal studies, it should be recognised when extending the results to the wider ice cap.

975

976 **References**

977 Calonne, N., Flin, F., Morin, S., Lesaffre, B., Rolland du Roscoat, S., & Geindreau, C.
978 (2011). Numerical and experimental investigations of the effective thermal conductivity of
979 snow. *Geophysical Research Letters, 38*(23), L23501. https://doi.org/10.1029/2011GL049234

980 Cuffey, K. M., & Paterson, W. S. B. (2010). *The physics of glaciers* (4th ed.). Academic
981 Press.

982 Dowdeswell, J. A., Drewry, D. J., Cooper, A. P. R., Gorman, M. R., Liestøl, O., & Orheim, O.
983 (1986). Digital mapping of the Nordaustlandet ice caps from airborne geophysical
984 investigations. *Annals of Glaciology, 8*, 51–58. https://doi.org/10.3189/S0260305500001130

985 Robin, G. de Q. (1955). Ice movements and temperature distribution in glaciers and ice
986 sheets. *Journal of Glaciology, 2*(18), 523-532. https://doi.org/10.3189/S0022143000017885

987 Schuler, T. V., Dunse, T., Østby, T. I., & Hagen, J. O. (2014). Meteorological conditions on an
988 Arctic ice cap-8 years of automatic weather station data from Austfonna, Svalbard.
989 *International Journal of Climatology, 34*(6), 2047-2058. https://doi.org/10.1002/joc.3821

990 Taurisano, A., Schuler, T. V., Hagen, J. O., Eiken, T., Loe, E., Melvold, K., & Kohler, J.
991 (2007). The distribution of snow accumulation across the Austfonna ice cap, Svalbard: Direct
992 measurements and modelling. *Polar Research, 26*, 7-13. https://doi.org/10.1111/j.1751-
993 8369.2007.00004.x

994

995

996